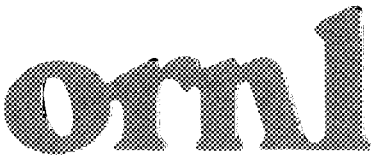

ORNL/TM-6926

OAK RIDGE NATIONAL LABORATORY

UNION CARBIDE

Experimental Study of Fission Counter Design Optimization with a Simplified Analytical Model of Performance

K. H. Valentine
J. T. De Lorenzo
W. T. Clay
V. K. Pare
G. C. Guerrant
R. S. Burns

OPERATED BY
UNION CARBIDE CORPORATION
FOR THE UNITED STATES
DEPARTMENT OF ENERGY

Printed in the United States of America. Available from
National Technical Information Service
U.S. Department of Commerce
5285 Port Royal Road, Springfield, Virginia 22161
NTIS price codes—Printed Copy: A05; Microfiche: A01

ORNL/TM-6926
Dist. Category
UC-79, -79m

Contract No. W-7405-eng-26

INSTRUMENTATION AND CONTROLS DIVISION

EXPERIMENTAL STUDY OF FISSION COUNTER DESIGN OPTIMIZATION WITH A SIMPLIFIED ANALYTICAL MODEL OF PERFORMANCE

K. H. Valentine, J. T. De Lorenzo,
W. T. Clay, V. K. Paré*
G. C. Guerrant, R. S. Burns*

---

*Present Address: P. O. Box 2175, Schlumberger Well Services, Houston, TX 77001.

Date Published - December, 1979

OAK RIDGE NATIONAL LABORATORY
Oak Ridge, Tennessee 37830
operated by
UNION CARBIDE CORPORATION
for the
DEPARTMENT OF ENERGY

HIGHLIGHTS

Careful specification of design variables is especially important for special-purpose fission counting applications such as high sensitivity [$\gtrsim$10 counts $s^{-1}(nv)^{-1}$] or operation in high gamma fields ($\gtrsim 10^5$ R/h). A computer code was developed to determine the combination of values of such variables as electrode spacing, filter time constants, and input cable impedance that would provide the best performance for a specified application. However, confident use of the code required validation of the assumptions and approximations on which it was based. To accomplish this validation, a variable-spacing fission counter was built and used in a parametric testing program to provide a well-characterized, experimental data base for comparison.

For maximum discrimination against gamma pileup, the variable-spacing counter was operated in the current-pulse mode during the tests. The variables which were considered are electrode spacing, interelectrode and electrode-to-ground capacitance, fill gas composition and pressure, characteristic impedance of the preamplifier input cable, filter time constants, the ratio of electric field to fill gas pressure (E/P, V cm^{-1} $torr^{-1}$), and gamma dose rate. For each combination of design variables, integral pulse height distributions were obtained for electronic preamplifier noise (EN) only, EN plus neutron excitation, and EN plus gamma excitation. A figure of merit was computed to characterize the performance of each experimental configuration. Qualitative trends of the figures of merit were supplemented and extrapolated through the use of a simplified analytical model of counter performance that was developed from equations of the computer code.

In some cases, the test data simply confirm previously known relationships between counter performance and such design variables as the E/P ratio and the product of fill gas pressure and electrode spacing. However, some data also show the influence of parameters not previously considered in detail, such as counter capacitance and impedance of the signal cable. In particular, the data show that for high-sensitivity counters with large electrode areas or for counters that must operate in very high gamma fields, substantial improvements

in performance can be obtained by lowering the characteristic impedance of the signal cables below the conventional 50 Ω value.

Validation of the computer code has not yet been completed. However, the agreement obtained between the experimental data and the simplified model provides at least partial validation of the basic mathematical concepts on which the code is based.

CONTENTS

1. INTRODUCTION

A variable spacing fission counter (VSC) was built and used in a parametric testing program to provide a well-characterized, experimental data base for validation of a fission counter design optimization code.[1] This validation was a prerequisite for application of the code to such optimization problems as minimizing the volume of a counter at constant sensitivity or maximizing the sensitivity at constant fissile inventory.

The original impetus for developing and validating the code arose from the need for a large-electrode-area fission counter having a neutron sensitivity of 5 to 10 counts $s^{-1}(nv)^{-1}$. Several applications of neutron monitoring in the Advanced Breeder Reactor program require neutron detectors that can detect neutrons with such high efficiency during simultaneous exposure to high gamma dose rates ($\sim 10^5$ R/h). Among these applications are delayed-neutron monitors for failed-element detection and location systems, ex-vessel low-level flux monitors for subcriticality measurements and source-range flux measurements, and subcriticality and fissile assay monitoring in fuel reprocessing plants. Since some of these applications may also require operation at elevated temperature, the relatively rugged construction, low susceptibility to radiation and temperature effects, and unsurpassed gamma discrimination capability of the fission counter make it a prime candidate. Since a neutron sensitivity of 10 counts $s^{-1}(nv)^{-1}$ is an order of magnitude increase over that obtained from commercially available fission counters, design problems such as alpha pileup and large interelectrode capacitance are substantially more severe than previously encountered. Consequently, design optimization is particularly important to the success of high-sensitivity counter designs.

For maximum discrimination against gamma pileup, the VSC was operated in the current pulse mode during the tests. The variables which were considered are electrode spacing, interelectrode and electrode-to-ground capacitance, fill gas composition and pressure, characteristic impedance of the preamplifier input cable, filter time constants, the ratio of electric field to fill gas pressure (E/P, V cm^{-1} $torr^{-1}$), and gamma dose rate.

The U_3O_8 coating thickness was not considered in these tests because large amounts of experimental data were already available concerning this important design variable.[2] For this report, the large amount of raw data accumulated (in the form of integral pulse height distributions) was reduced by computing a "figure of merit" to characterize the performance of each experimental configuration studied. Further use of the word "data," therefore, refers to these figures of merit. In some cases, we arranged the data to show some important relationships between fission counter performance and specific design variables. In other cases, we used a simple, analytical model of fission counter performance to extrapolate qualitative performance trends beyond the range of our measurements. While not as detailed as the simulation code, the analytic model has the advantage that the descriptive equations can be written in closed form, and, therefore, they are amenable to exact solution for the maxima or optima.

2. BACKGROUND

The initial objective of the test program was to verify a design optimization code so that it could be used to aid in the design of a high-sensitivity fission counter having a sensitivity of 5 to 10 counts $s^{-1}(nv)^{-1}$. Comparisons of initial test results with predictions of the code were not encouraging, but they did point out several areas where oversimplified approximations had been used. The program was continuously modified as more experimental data became available, but still it was not considered to be a reliable design tool by the time program schedules required design specifications for the high-sensitivity counter.

We therefore relied on the experimental approach and shifted the emphasis of the testing program to designs involving high interelectrode capacitance which would be inherent in a large fission counter. These high capacitance tests, in conjunction with qualitative trends predicted by the code, were then used as a basis for a tentative, high-sensitivity design. In most instances where the data are incomplete or inconclusive, we attribute these deficiencies to this major change in objective midway through the testing program.

3. DESCRIPTION OF THE FISSION COUNTER ASSEMBLY

The variable spacing fission counter (Fig. 1) was a parallel-circular-plate device designed for underwater gamma testing at room temperature. It consisted of two separate parts: a counter and a cable-header. This design facilitated the task of implementing variations in the cable characteristic impedance, extra interelectrode capacitance, and the gas type and pressure.

3.1 Fission Counter

The fission counter had 28 electrodes (6.35 cm OD), each of which was coated with U_3O_8 (99.9% enriched ^{235}U) to a thickness of 2 mg/cm^2; the total electroplated area was $\sim$1470 cm^2. The 28 electrodes were divided evenly between two sets and stacked alternately with spacers onto six tie rods, three per set. Each set was electrically insulated from the other set and connected to its particular ceramic feedthrough at the cable end of the counter. The tie rods were rigidly supported at each end by a ceramic insulator. The lengths of the tie rod end-spacers were such that the center of the sensitive volume remained stationary regardless of the electrode spacing.

For high common-mode rejection of electromagnetic interference, the counter was operated differentially by connecting each electrode set to one of the inputs of an ORNL Q-5095 differential preamplifier. The high voltage (ΔV) was divided evenly ($\pm 1/2\ \Delta V$) between the two sets of electrodes (via the two cables) to reduce the probability of breakdown pulse noise.

3.2 Cable Header

The header was attached to the top of the counter with screws, alignment pins, and an O-ring to provide a watertight enclosure. Space inside the header was used to install capacitors to add interelectrode capacitances (for the simulation of larger counters) and to make cable connections to the counter electrodes.

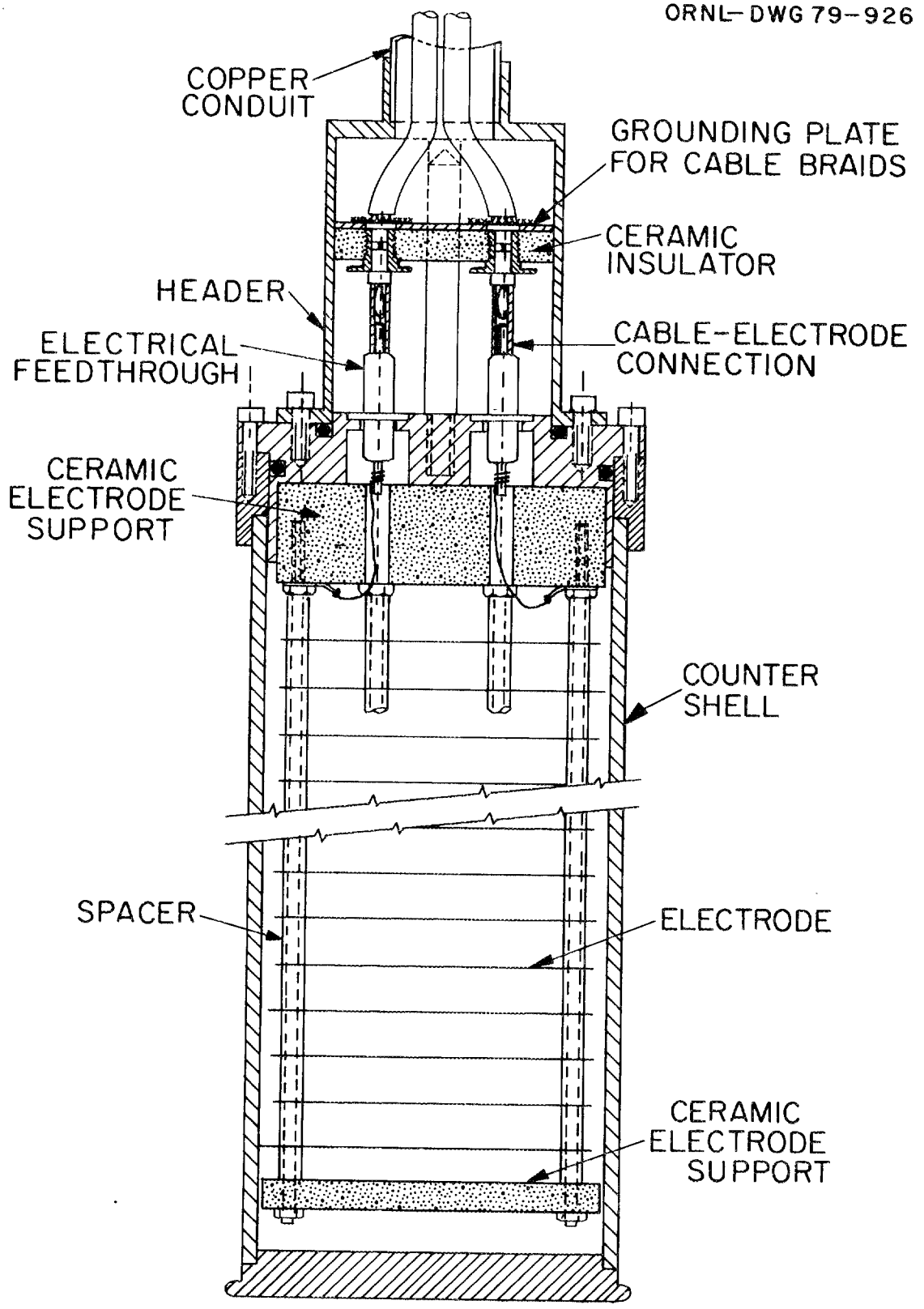

Fig. 1. Cross-sectional view of experimental, variable-spacing fission counter. (Counter shell is ∿8 cm diam and ∿32 cm long.)

Eight lengths of RG-223/U, double-shielded, 50-Ω coaxial cable entered the header through a 3/4-in.-diam by 21-ft-long copper tube that was hard-soldered to the header. Parallel combinations of one to four cables provided characteristic cable impedances of 50, 25, 16.7, and 12.5 Ω for each electrode set. The far end of the copper tube was flanged for connection to an outer shield box for the preamplifier.

4. ELECTRONIC COUNTING CHANNEL

Figure 2 illustrates the parallel cable connections, and Fig. 3 is a diagram of the complete counting channel. Two supplies applied half the total collecting voltage to each set of electrodes so as to minimize the magnitude of the dc voltage on the cables and the bias supply filters. The preamplifier[3] had a differential gain of 500 and a rise time of 5 ns. An additional gain of ∿100 in the three main amplifier stages increased the signal above the 30-mV lower limit of the leading-edge pulse discriminator (ORNL Q-5480).[4]

Each main amplifier stage had a bandwidth of dc to 150 MHz, and the discriminator had a pulse-pair resolution of <10 ns. The bandwidth of the system was limited by interstage, single-pole, low- and high-pass (RC-CR) filters with selectable time constants of 13.5, 27, 50, 100, 150, and 200 ns. A second RC filter (2 ns) suppressed a parasitic resonance in the RC-CR filter networks.

The threshold level of the pulse discriminator was set by the output of a digital-to-analog converter (DAC) under control of an automated data acquisition system. The usable threshold was between 30 mV and 1.0 V. The lower limit was determined by the stability and sensitivity of the discriminator; the upper limit, by the linearity of the main amplifier. The DAC output resolution was 10 mV (10 V maximum). The output of a precision dc attenuator (10X) was applied to the discriminator.

Near the end of their work with the variable spacing counter, the authors redesigned the discriminator to include a "window" mode. The window was adjustable to 100 mV maximum.

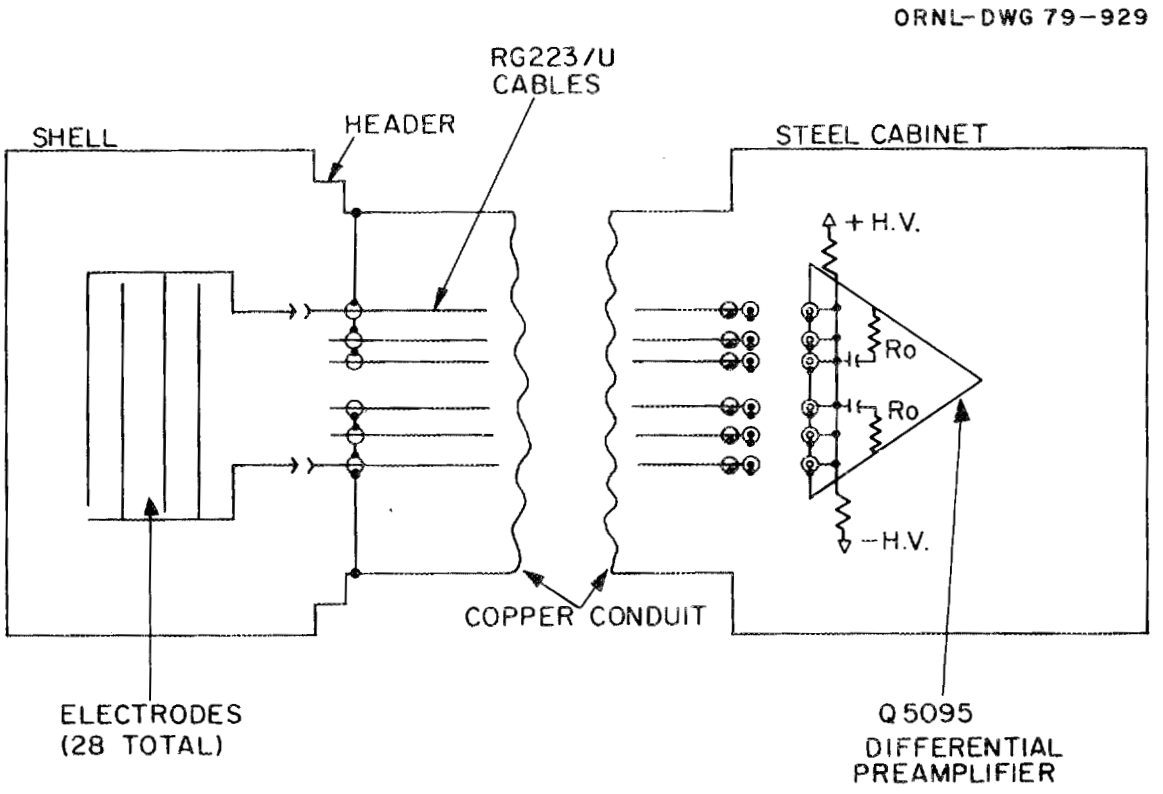

Fig. 2. Electrical connections for the variable-spacing counter and Q-5075 differential preamplifier. (R_o is matched to the input cable; only six signal cables are shown.)

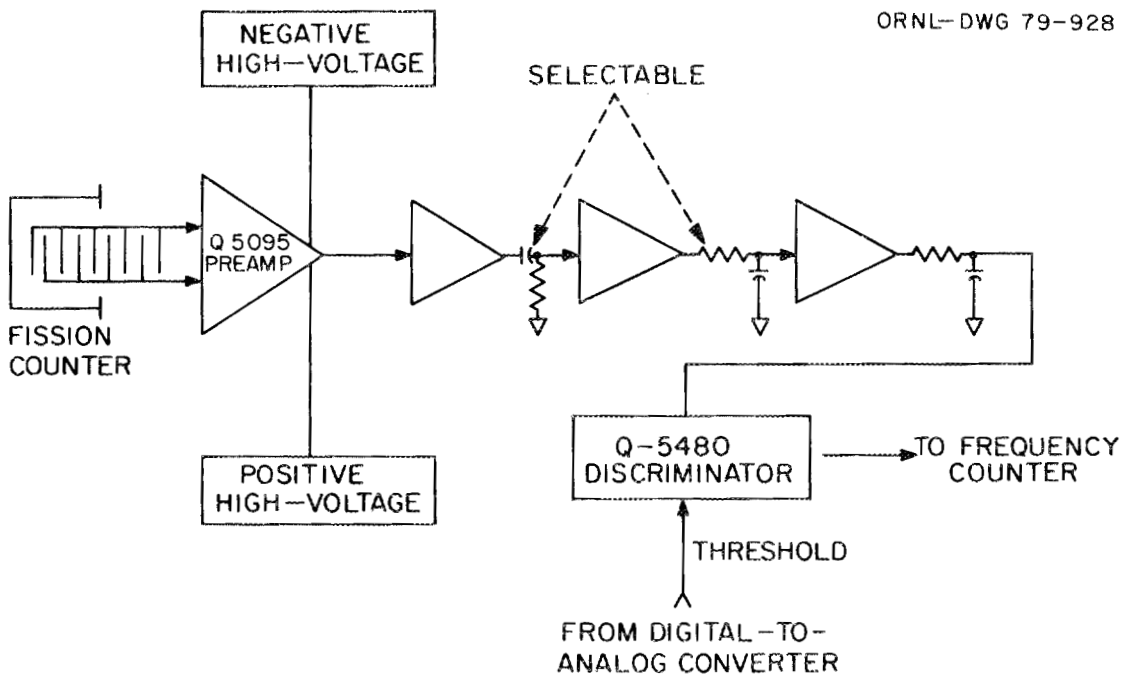

Fig. 3. Diagram of the electronic counting channel.

5. DATA ACQUISITION SYSTEM

A diagram of the data acquisition system is shown in Fig. 4. The output of the discriminator was the input to the frequency counter. A thermal printer made hard copies of the experimental data, and a cassette recorder made tapes of the data for subsequent data retrieval and analysis. Integral and differential bias curves were plotted by an x-y plotter.

Data acquisition was based on a cycle time of ∿10 s. At the beginning of the first cycle, the calculator set the initial threshold of the programmable discriminator and then enabled the frequency counter. After 10 s of data acquisition, the frequency counter was disabled, and its data were transferred to the calculator memory. The threshold was then increased by a preset increment, and the cycle was repeated.

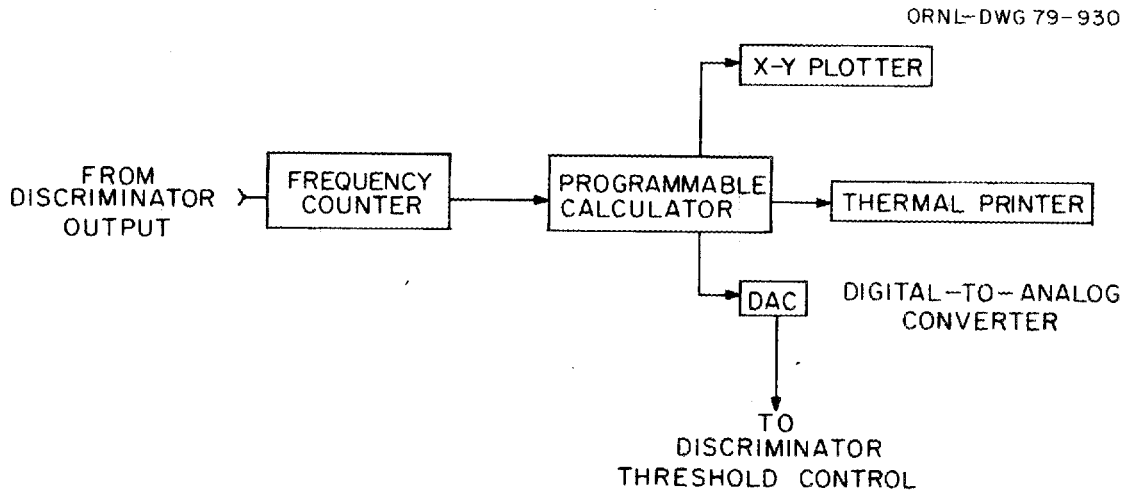

Fig. 4. Diagram of the data acquisition system.

The pulse height calibration of the system was checked daily, using precision pulses from a mercury-relay pulse generator. Under control of the programmable calculator, the half-trigger levels* for input pulses of three different amplitudes were obtained, and a linearity curve was calculated from a first-order fit. The curve was normalized to express both integral and differential bias plots in terms of arbitrary, but reproducible, pulse height (PHS) units. This procedure removed all dependence of experimental data on the long-term drifts of electronic gain or discriminator threshold sensitivity and offset.

For practical considerations, the calibration test pulse had a fixed shape: ~10 ns rise time and a 600-μs exponential tail. However, when the current pulse from a fission counter was processed, the output pulse amplitude depended on the shape, as well as the amplitude, of the current pulse. Thus, each variable-spacing design resulted in different, peak pulse amplitudes and variations in integral and differential bias plots, even though the normalized PHS units were used. Therefore, to give a convenient means of comparing the performance of various counter designs, the plots were made with a logarithmic pulse height scale so that only a simple horizontal displacement of the bias curves quickly revealed the counter configuration with the superior rejection of system noise.

6. GROUNDING AND SHIELDING

A copper conduit enclosed the eight double-shielded RG-223/U coaxial cables and connected the header of the variable spacing counter to the outer shield box of the preamplifier. The copper conduit was hard-soldered to the header, and, as constructed, the shields of the signal cables were also electrically connected to the header. Thus, the shielding and grounding at this point differed from the classic design which

---

*The system differential response to a calibration pulse was modulated by preamplifier noise and appeared as a Gaussian pulse height distribution whose centroid corresponded exactly to the calibration pulse amplitude. Therefore, in the integral mode, we searched for the discriminator level which resulted in a trigger rate equal to one-half of the pulse generator frequency.

insulates the outer (or "dirty") shield from the inner (or "clean") signal shield to avoid a ground loop. (Our experience at ORNL has shown that balanced input systems are more tolerant of ground loops and can simplify the design of the detector.)

Electromagnetic interference from the data acquisition equipment and its associated interface bus system created counting errors. Since a shielded enclosure was not practicable, the electromagnetic interference was effectively reduced by connecting all components of the data acquisition system to a ground plane with short lengths of shielding braid. The ground plane was fabricated from a 3 × 4 ft sheet of copper-clad epoxy board.

7. TEST FACILITIES

7.1 Gamma Irradiation Test Facility

The gamma facility consisted essentially of a water-filled thimble that extended from the surface of a water-filled canal to its bottom, where a gamma source holder was positioned. The holder accommodated up to 12 ^{60}Co pencils, each ∿15,000 Ci, in a radially symmetric array. Water between the thimble and the holder was enclosed by a caisson; the water could be pneumatically ejected to cause higher gamma dose rates than would have been obtainable otherwise. The thimble water was isolated from the slightly contaminated canal water, and the counter was inserted and withdrawn without removing the gamma sources.

7.2 Neutron Testing Geometry

The neutron testing geometry (ORNL Q-2633) was a cylindrical block of high-density polyethylene, ∿81 cm long by 61 cm diam. The block had a central, axial hole to hold the neutron source, and another axial cavity at midradius for the test counter. Count rates of about 10^4 neutrons/s were obtained from the variable spacing counter with a Pu-Be source that generated 8×10^6 neutrons/s.

8. MATHEMATICAL MODEL OF FISSION COUNTER PERFORMANCE

The experimental data in the following section clearly show that the performance of a fission counter operating in the current pulse mode is sensitive to changes of such design variables as electrode spacing, cable impedance, and electron drift velocity. However, in many cases the data are not complete enough to predict even qualitative performance trends outside the experimental ranges. Therefore, this section presents a relatively simple model of fission counter performance that will help fill some of the experimental gaps and serve as a reference for subsequent interpretation of the data.

Figure 5 is a diagram of the simplest model of a current pulse fission counting channel that can be expected to yield useful analytical results. It consists of a parallel-plate fission counter having a total coated electrode area A and an electrode spacing D. The signal electrode is connected to a current-sensitive preamplifier by a transmission line having a characteristic impedance of Z_0 Ω and terminated by the input impedance of the preamplifier at Z_0 Ω. Since we assume that the noise spectrum of the preamplifier is white, a single-pole, low-pass filter with a time constant of $\tau_f = R_f C_f$ is included to keep the total noise finite. A limiting value for this time constant is inherent in any physical system because the bandwidth of the preamplifier is finite.

In this model, alpha pulses resulting from uranium decay are assumed to be well piled up and can therefore be characterized with an equivalent gamma dose rate. For some design problems, the mean time between alpha pulses is comparable to the resolving time of the counting channel, and more sophisticated probability models are needed to accurately treat the pileup process.

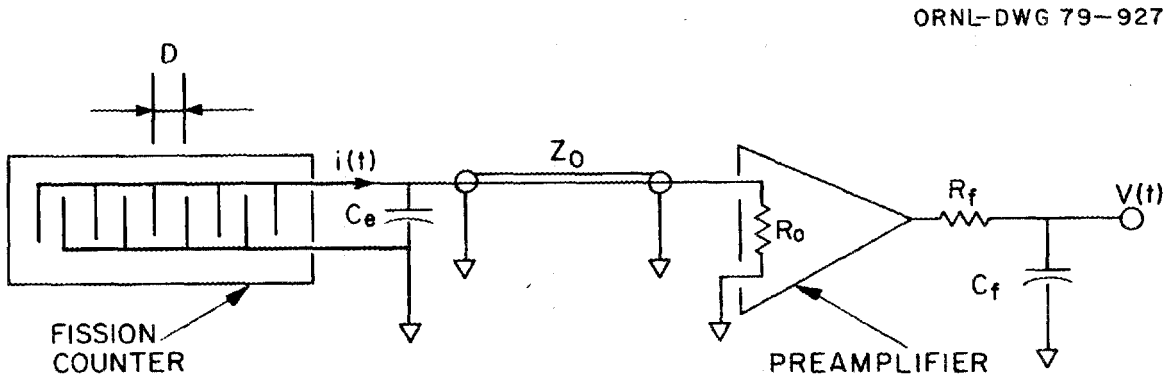

Fig. 5. Model of fission counting channel for mathematical analysis.

Symbols used in the following mathematical development are defined below.

ε_o Permittivity of free space (8.85×10^{-12} F/m)

A Total coated electrode area (m^2)

v_d Electron drift velocity (m/s)

Z_0 Characteristic cable impedance (Ω)

D Electrode spacing (m)

C_e Interelectrode capacitance, equals $\varepsilon_o A/(2D)$, (F)

q_n Charge deposited in fill gas by a neutron event (C)

σ_{e0}^2 Zero frequency value of the auto-power spectral density (APSD) of the noise current (A^2/radian)

σ_{p0}^2 Zero frequency value of the APSD of the current due to alpha and gamma pileup (A^2/radian)

σ_t Total rms noise current (A)

τ_i Inherent integration time constant, $Z_0 C_e = \frac{\varepsilon_o A Z_0}{2D}$, (s)

τ_f Low-pass filter time constant, equals $R_f C_f$, (s)

t_c Electron collection time, equals D/V_d, (s)

τ' $(\tau_i \tau_f)/(\tau_i - \tau_f)$, (s)

τ_0 Characteristic time, equals $\sqrt{\frac{\varepsilon_o A Z_0}{2 v_d}}$, (s)

D_0 Characteristic length, equals $v_d \tau_0 = \sqrt{1/2\ \varepsilon_o A v_d Z_0}$, (m)

α Dimensionless electrode spacing, equals D/D_0

β Dimensionless, low-pass filter breakfrequency, equals τ_0/τ_f

G Preamplifier gain (V/A).

The first step of this analysis will be to formulate a figure of merit for fission counter performance that can be handled analytically. For this purpose, we define the figure of merit μ', as $\mu' = V_M/V_l$, where V_M is the peak voltage at the discriminator input that results from a neutron event, and V_l is the discriminator setting required to reduce the count rate due to all noise sources to less than 1 count/s.

The second step will be to select pulse shapes for the calculations of V_M and V_l. Since the typical areal fill-gas density for a fission counter is about 1 mg/cm^2, an electron needs only about 20 keV of energy to traverse the interelectrode gap. In a typical gamma field produced by ^{60}Co sources or by fission product decay, the energy of a large fraction of the photo and Compton electrons created in the fission counter is >20 keV; therefore, most gamma events will produce a reasonably uniform ionization density across the interelectrode gap, and the shape of the resulting current pulses will be triangular.

Since the range of a fission fragment in argon is 3-4 mg/cm^2, the discussion of the preceding paragraph could also be applied to fission events. However, for the purpose of maximizing the neutron count rate (i.e., optimizing the counter), the shape of current pulses which are barely capable of triggering the discriminator is a more important consideration than the shape of the most probable current pulse.

The most energetic current pulse results when a fission fragment is emitted from the front surface of the neutron-sensitive coating of a negative electrode; the fragment's trajectory is nearly parallel to the plane of the electrode. In this case, the shape of the current pulse is approximately rectangular. Thus, if V_1 is large (compared to the neutron pulse height spectrum), the counter should be optimized for rectangular pulses.

Emission of low-energy fission fragments with very short residual ranges in the interelectrode gap produces low-amplitude current pulses. If emission occurs from the positive electrode, the pulse shape is approximately an impulse with minimum total energy; but, if emission is from the negative electrode, the pulse shape is approximately rectangular. In this case, it is probably advisable to sacrifice the low-energy impulses and to optimize the counter for rectangular pulses.

Since heuristic arguments can be made in favor of the rectangular neutron pulse at both low and high values of V_1, the rectangular shape is assumed in the following derivations, even though the same type of arguments probably indicate that a triangular shape would be appropriate for intermediate values of V_1.

The time dependence of the fission counter signal is

$$i(t) = \begin{cases} \dfrac{q_n}{t_c}, \text{ for } 0 \leq t \leq t_c , & \text{(1a)} \\ 0, \text{ otherwise.} & \text{(1b)} \end{cases}$$

After two single-pole integrations with time constants of τ_i and τ_f ($\tau_i \neq \tau_f$), the voltage pulse becomes

$$V(t) = \begin{cases} \dfrac{Gq_n}{t_c}\left[1 - \dfrac{\tau'}{\tau_f}e^{-t/\tau_i} + \left(\dfrac{\tau'}{\tau_f} - 1\right)e^{-t/\tau_f}\right], \text{ for } 0 \le t \le t_c, & (2a) \\ \dfrac{Gq_n}{t_c}\left[\dfrac{\tau'}{\tau_f}\left(e^{t_c/\tau_i} - 1\right)e^{-t/\tau_i} - \left(\dfrac{\tau'}{\tau_f} - 1\right)\left(e^{t_c/\tau_f} - 1\right)e^{-t/\tau_f}\right], & (2b) \\ \text{otherwise.} \end{cases}$$

Since the peak of the voltage pulse always occurs with $t \geq t_c$, the value of t that maximizes V(t) is found from Eq. (2b) by setting

$$\left.\frac{\partial V(t)}{\partial t}\right|_{t_m} = 0 \ . \qquad (3)$$

The solution is

$$t_m = \tau' \ell n\left(\frac{e^{t_c/\tau_f} - 1}{e^{t_c/\tau_i} - 1}\right). \qquad (4)$$

Back substitution of Eq. (4) into Eq. (2) yields

$$V_m = V(t_m) = \frac{Gq_n\left(e^{t_c/\tau_i} - 1\right)^{\tau'/\tau_f}}{t_c\left(e^{t_c/\tau_f} - 1\right)^{\tau'/\tau_i}} \ . \qquad (5)$$

The integral bias curve for all noise sources[1] is

$$C_t(V) = f_R e^{-V^2/2\sigma_t^2} \ . \qquad (6)$$

Setting the left-hand side of Eq. (6) equal to 1 and solving for V yields

$$V_1 = \sigma_t\sqrt{2\ell n(f_R)} \ . \qquad (7)$$

Although f_R is a function of counter design and noise intensity, V_1 depends only on the square root of the logarithm of f_R. For the present, V_1 will be approximated as

$$V_1 = k\sigma_t \ , \tag{8}$$

where k is a constant. Since electronic noise sources and pileup noise sources are uncorrelated, Eq. (8) can be rewritten as

$$V_1 = k\left(\sigma_e^2 + \sigma_p^2\right)^{1/2} \ . \tag{9}$$

With the assumption of a white electronic noise spectrum, the electronic noise power spectral density is constant σ_{e0}^2 , and the rms electronic noise at the output is calculated as

$$\sigma_e^2 = G^2 \int_0^\infty \frac{\sigma_{e0}^2 \, d\omega}{1 + \omega^2 \tau_f^2} = \frac{\pi G^2 \sigma_{e0}^2}{2\tau_f} \ . \tag{10}$$

With an assumption that the triangular-shaped gamma current pulses are of the form

$$i_\gamma(t) = \begin{cases} \dfrac{q_\gamma}{t_c}\left(1 - \dfrac{t}{t_c}\right), & \text{for } 0 \le t \le t_c \\ 0, & \text{otherwise,} \end{cases} \tag{11a}$$

the power spectral density of the pileup noise becomes

$$P(\omega) = 2\nu \left| \int_0^{t_c} \frac{q_\gamma}{t_c}\left(1 - \frac{t}{t_c}\right) e^{-i\omega t} \, dt \right|^2$$

$$= \frac{4\sigma_{p0}^2}{\omega^2 t_c^2} \left\{ 1 - \frac{2 \sin\left(\omega t_c\right)}{\omega t_c} + \frac{2\left[1 - \cos\left(\omega t_c\right)\right]}{\omega^2 t_c^2} \right\} , \tag{12}$$

where ν and q_γ are the gamma-ray interaction rate and average charge per interation, respectively;

and the rms pileup noise is calculated as

$$\sigma_p^2 = G^2 \int_0^\infty \frac{P(\omega)\, d\omega}{\left(1 + \omega^2\tau_f^2\right)\left(1 + \omega^2\tau_i^2\right)}$$

$$= \frac{2\pi G^2 \sigma_{p0}^2}{t_c} \left[\frac{2}{3} - \frac{\tau_i^3}{t_c^3} \frac{t_c^2 - 2\tau_i^2 + 2\tau_i\left(\tau_i + t_c\right) e^{-t_c/\tau_i}}{\tau_i^2 - \tau_f^2} \right.$$

$$\left. + \frac{\tau_f^3}{} \frac{t_c^2 - 2\tau_f^2 + 2\tau_f\left(\tau_f + t_c\right) e^{-t_c/\tau_f}}{\tau_i^2 - \tau_f^2} \right]. \qquad (13)$$

In terms of the dimensionless variables, α and β, Eq. (9) can be written as

$$V_1 = kG\, \sigma_{e0} \left(\frac{\pi}{2\tau_0}\right)^{1/2} \left\{ \beta + \left(\frac{\sigma_{p0}}{\sigma_{e0}}\right)^2 \right.$$

$$\left. \frac{4}{\alpha} \left[\frac{2}{3} - \frac{\beta^2}{\beta^2 - \alpha^2} \frac{\alpha^4 - 2 + 2\left(1 + \alpha^2\right) e^{-\alpha^2}}{\alpha^6} \right.\right.$$

$$\left.\left. + \frac{\alpha^2}{\beta^2 - \alpha^2} \frac{\alpha^2\beta^2 - 2 + 2\left(1 + \alpha\beta\right) e^{-\alpha\beta}}{\alpha^3\beta^3} \right] \right\}^{1/2} \qquad (14)$$

$$\equiv kG\, \sigma_{e0} \left(\frac{\pi}{2\tau_0}\right)^{1/2} \left\{ \beta + \left(\frac{\sigma_{p0}}{\sigma_{e0}}\right)^2 F(\alpha,\beta) \right\}^{1/2}.$$

With substitution of α and β in Eq. (5), the expression for the figure of merit becomes

$$\mu' = \frac{V_m}{V_1}$$

$$= \left\{ \frac{q_n}{k\sigma_{e0}\tau_0^{1/2}} \right\} \left\{ \frac{\sqrt{\frac{2}{\pi}} \left[\frac{\left(e^{\alpha^2} - 1\right)^{\beta}}{\left(e^{\alpha\beta} - 1\right)^{\alpha}} \right]^{\frac{1}{\beta - \alpha}}}{\alpha\beta \left[1 + \left(\frac{\sigma_{p0}}{\sigma_{e0}} \right)^2 F(\alpha,\beta)/\beta \right]^{1/2}} \right\} . \qquad (15)$$

9. TEST RESULTS

The general format of the testing program was, first, to establish an experimental configuration consisting of some unique combination of design variables. Next, the automatic data acquisition system measured and recorded integral bias curves for electronic plus alpha pileup noise (EN) only, EN plus 1.6×10^6 R/h gamma pileup, and EN plus neutron counts. A few tests were also made in a gamma field near 7×10^6 R/h. However, since at this dose rate, saturation could be obtained only at the smallest electrode spacings and the lowest fill gas pressures, the results were generally poor. Data taken at unsaturated conditions, which would be of interest to designers, were not obtained, since the neutron and gamma responses were measured separately.

Much of the test data presented pertain to an arbitrary value of counter capacitance of ∿270 pF and are intended to show trends of the figure of merit rather than to represent the specific designs of a high-sensitivity fission counter. The 1.6×10^6 R/h gamma field used for the majority of the testing was arbitrarily chosen to provide a response well above electronic plus alpha pileup noise. The resulting gamma pileup noise was about 2.5 times greater than that expected for a high-sensitivity counter in a 10^5 R/h field; however, the scaling laws are well understood,[1] and performance at the lower dose rate can be accurately extrapolated.

In some cases, the test data simply confirm previously known relationships between counter performance and such design variables as the E/P ratio and gas pressure.[5] However, some data also show the influence of

parameters not previously considered in detail, such as counter capacitance and impedance of the signal cable.

9.1 Definition and Computation of the Figure of Merit

The method for computing μ-values from experimental data is illustrated in Fig. 6. The curve labeled $C_\gamma(V)$ is a least-squares fit of

$$C_\gamma(V) = f_R e^{-V^2/2\sigma^2} , \tag{17}$$

where $C_\gamma(V)$ is the number of pulses per second that will trigger an integral discriminator with a threshold setting of V, and f_R and σ are constants for a given counting channel design and gamma field. The curve labeled $C_n(V)$ is a local,* second-order polynomial fit to integral pulse height data for neutrons only. The value $C_n(V_1)$ is obtained by extending a vertical line from the 1-count/s intercept of the C_γ curve to the C_n curve. The value of the ordinate at the resulting intersection is $C_n(V_1)$. The value of $C_n(0)$ can be approximated by ignoring electronic noise and graphically extrapolating the neutron data to zero pulse height. However, the accuracy of this method requires knowledge of the behavior of the integral bias curve near zero pulse height. This uncertainty is almost entirely eliminated by using the computer simulation code to compute the integral pulse height response that would be obtained in the absence of noise. After overlaying and visually aligning the computed and experimental curves, we obtain $C_n(0)$ as the intersection of the computed curve with the experimental ordinate. The value of $C_n(0)$ obtained this way is applicable as long as the sensitive volume remains fixed with respect to the neutron field. In addition, this same value remains applicable as the electrode spacing is varied if the axial flux gradient is constant over the sensitive length (as is the case in the neutron testing geometry).

---

*No simple analog to Eq. (17) exists for the neutron integral, pulse height distribution. Thus, we arbitrarily chose a second-order polynomial to approximate the curve over a limited pulse height range.

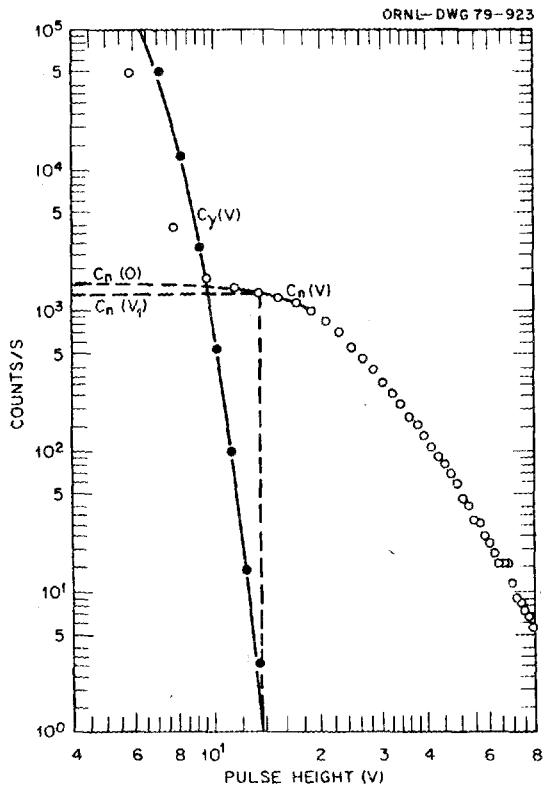

Fig. 6. Integral pulse height distribution with constructions for determination of experimental figure of merit.

A convenient method for comparing different counting channel configurations is to characterize the performance of each channel with a single number called a "figure of merit." In this section, the figure of merit (μ) is defined as

$$\mu = \frac{C_n(V_1)}{C_n(0)} , \tag{16}$$

where $C_n(0)$ is the neutron count rate that would be obtained at a discriminator threshold of zero in the absence of noise, and V_1 is the threshold required to reduce the spurious count rate due to all noise sources (including gamma pileup when present) to less than 1 count/s. The range of μ is $0 \leq \mu \leq 1$, and μ is an implicit function of gamma dose rate, since V_1 increases as the gamma dose rate increases. Also, μ may be interpreted as the fraction of theoretically detectable fission events that result in pulses at the discriminator; μ is directly proportional to neutron sensitivity.

Although this measure of performance is different from that presented in the preceding analytical section, our experience is that they exhibit similar qualitative trends, as might be expected since the neutron integral pulse height distribution is inherently monotonic and smoothly varying.

9.2 Electrode Spacing

Electrode spacing is the most important parameter to optimize since, except for special devices like the one used in this work, it cannot be changed without rebuilding or replacing the entire counter. Since information for designing a high-sensitivity counter was needed, the large counter was simulated at each electrode spacing by adjusting its interelectrode and stray capacitances with padding capacitors to give values consistent with the large electrode area of a 10 count sec^{-1} $(nv)^{-1}$ design. These data are presented here, rather than data for the arbitrary value of ∿270 pF, because of their relevance to the proposed design.

Figure 7 shows the effect of electrode spacing on the figure of merit, with the product of gas pressure (P) and spacing (D) held constant at 290 torr-cm of an Ar - 5% CO_2 gas mixture, and the E/P ratio held constant at 1.38 V cm^{-1} $torr^{-1}$. This approach assures nearly equal charge generation in the interelectrode gap and equal drift velocities for all values of electrode spacing. Under these conditions, the collection time is directly proportional to the spacing, and the current pulse amplitude is inversely proportional to the spacing. The E/P value of 1.38 used to obtain the data of Fig. 7 provided an operating point on the slowly varying portion of the electron drift velocity curve. The data were taken at three values of cable impedance (50, 25, and 16.7 Ω) and three values of RC-CR filter time constants (50, 27, and 13.5 ns). Some data were also taken at a cable impedance of 12.5 Ω, but the results were so poor that tests at this impedance were discontinued and none of these data are presented here.

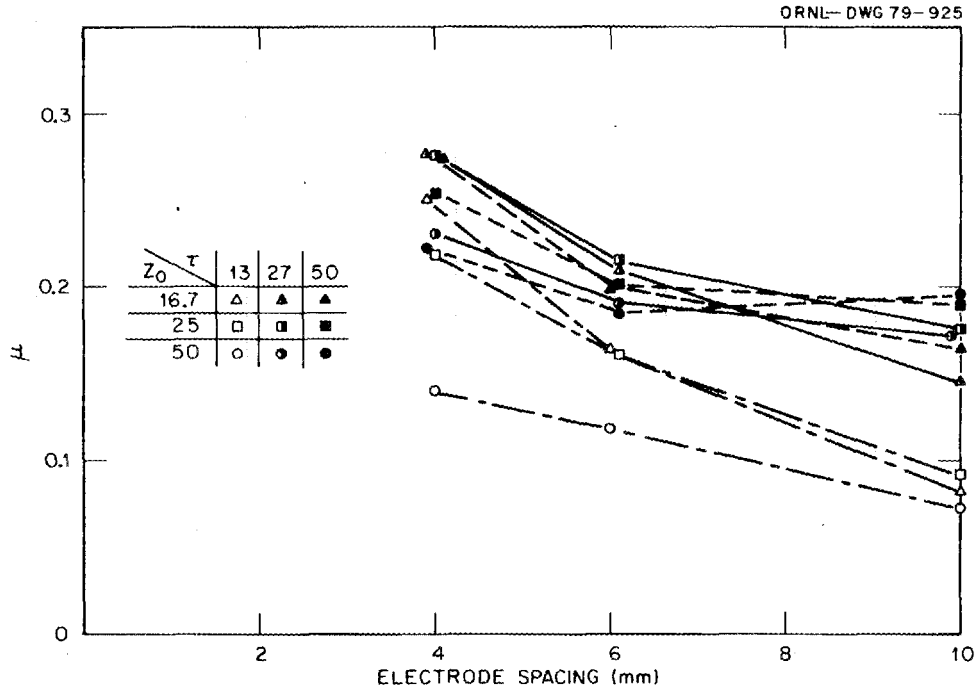

Fig. 7. Experimental figure of merit versus electrode spacing for various combinations of cable impedance and filter time constant $\left(\text{Ar} - 5\%\ \text{CO}_2,\ 1.6 \times 10^6\ \text{R/h},\ \text{E/P} = 1.38\ \text{V torr}^{-1}\ \text{cm}^{-1}\right)$.

We attribute the decrease of figure of merit values from their values at the 4-mm spacing to the larger collection times, which reduces the current pulse amplitude of a neutron event to a greater extent than the gamma pileup noise, resulting in a lower signal-to-noise ratio. The figure of merit for the 50-Ω, 50-ns case at the 10-mm spacing is anomalously high. This is the only instance where the figure of merit increases with spacing. We believe that this behavior was due to incomplete saturation, resulting in an erroneously low gamma pileup. Since saturation is not a function of the cable impedance or the filter time constant, the other data at the 10-mm spacing must be similarly affected.

The figure of merit values are also expected to decrease for small spacing because of the resulting, large interelectrode capacitance. Although our data do not extend to spacings that are small enough to show this decrease, it can be predicted with the analytical approach of Sect. 8 by evaluating Eq. (15) at different values of α while holding the other variables constant. Some results are shown in Fig. 8, where the values of τ_0, D_0, β, σ_{e0}, and σ_{p0} were chosen to simulate the experimental configurations used to obtain the data of Fig. 7 with $\tau_f = 27$ ns.

Figure 8 shows that Eq. (15) predicts a peak which is followed by a monotonic decline in the figure of merit as the electrode spacing is decreased. It is also seen that the value of cable impedance which provides the best performance increases as the electrode spacing (and thus the collection time) increases. This trend is also evident in the data of Fig. 7.

The predicted values of electrode spacing that correspond to maxima in the figures of merit are somewhat larger than might be inferred from Fig 7. We attribute this discrepancy to the omission of the differentiator in the mathematical treatment. When the differentiator is included in the analysis,* the qualitative predictions are similar to those of the simplified model presented here, but as might be expected, quantitative agreement with the experimental data is much improved.

9.3 Areal Gas Density (PD Product)

The effect of the PD product (gas pressure × spacing) was examined by varying the pressure of an Ar - 5% CO_2 gas mixture in a test counter with a fixed spacing of 4 mm, a constant E/P ratio of 1.38, and a constant capacitance of 270 pF. Measurements were made at three pressures, 724, 1145, and 1810 torr; they were repeated at three cable impedances of 16.7, 25, and 50 Ω and three RC-CR filter time constants of 13.5, 27, and 50 ns.

These data are plotted in Fig. 9, and the 25- and 50-Ω curves show a monotonic increase in figure of merit values as the gas pressure is reduced. We attribute this gain of performance at lower pressures to the different specific ionization characteristics (dE/dx) of fission fragments and energetic electrons which cause both the neutron and gamma ionization to decrease in such a manner that the neutron-to-gamma-charge ratio increases. The optimum fill gas pressure will therefore decrease with increasing gamma dose rate. However, continuing to lower the pressure will ultimately result in dominance of electronic noise (which is not affected

---

*To be published.

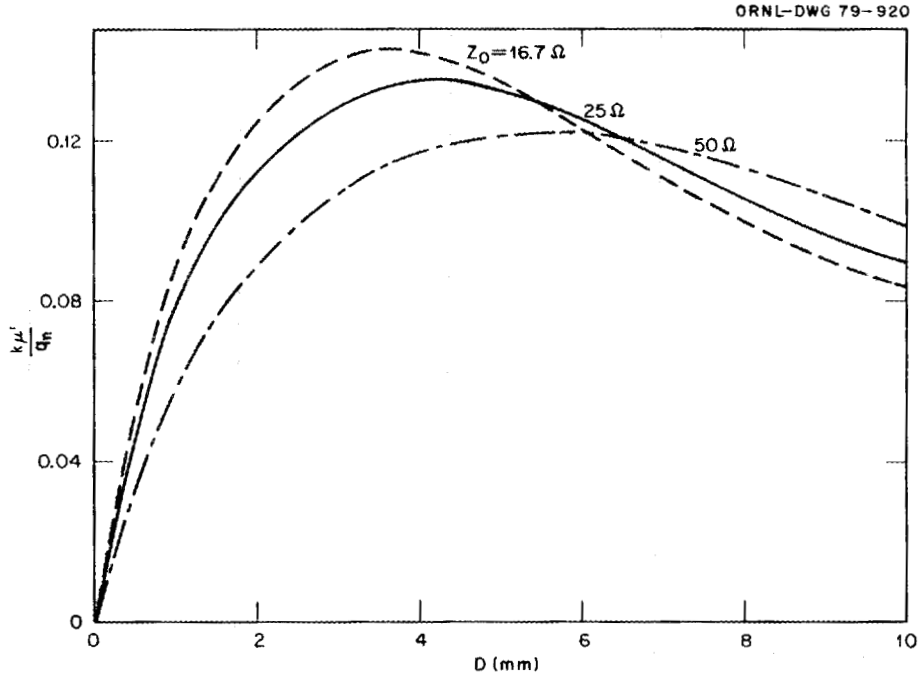

Fig. 8. Predicted dependence of figure of merit on electrode spacing.

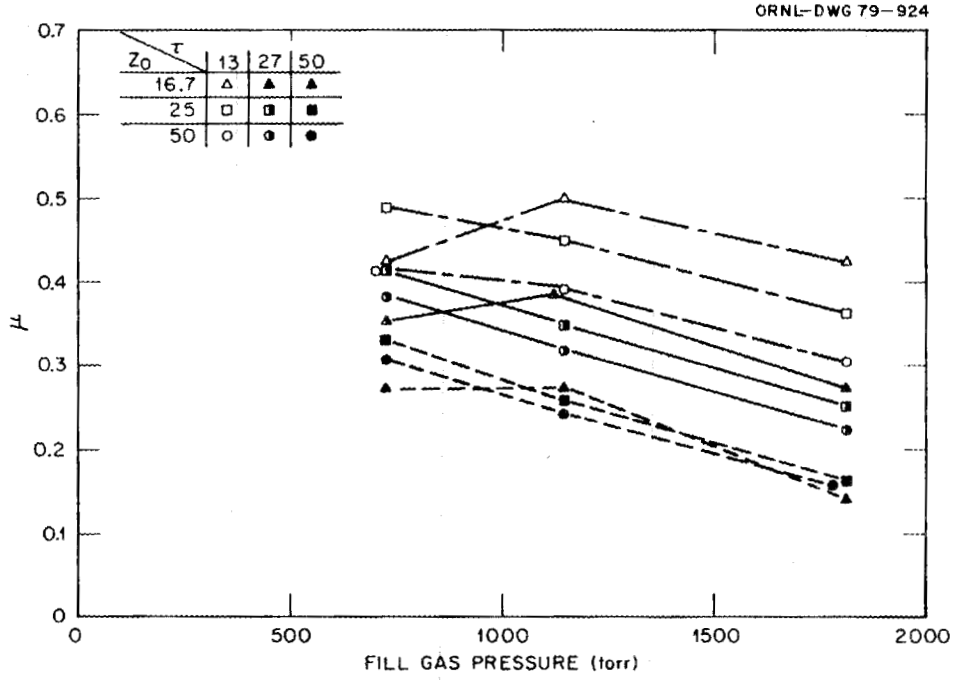

Fig. 9. Experimental figure of merit versus fill gas pressure (or PD product) for various combinations of cable impedance and filter time constant $\left(\text{Ar - 5\% } CO_2,\ 1.6 \times 10^6 \text{ R/h},\ E/p = 1.38 \text{ V torr}^{-1} \text{ cm}^{-1},\ D = 4 \text{ mm}\right)$.

by pressure), producing a peak and decline of the figure of merit. This effect can also be predicted from Eq. (15) by noting that only the variables q_n and σ_{p0} are functions of gas pressure. When gamma noise dominates ($\sigma_{p0}/\sigma_{e0} >> 1$), μ' is proportional to q_n/σ_{p0}; when electronic noise dominates ($\sigma_{p0}/\sigma_{e0} << 1$), μ' is proportional to q_n/σ_{e0}. For the preamplifier[6] used in these tests, which had a grounded-base input stage, there was a characteristic increase in electronic noise as the input impedance of the preamplifier was reduced. With a 16.7-Ω input cable, the electronic noise level was high enough to influence the figure of merit even at pressures of 1000 torr.

9.4 Cable Impedance and Counter Capacitance

In conjunction with the counter capacitance, the cable impedance forms a single-pole, low-pass filter which can influence the counting channel performance when its time constant ($C_c Z_0$) becomes significant compared with the electron collection time, as in a large-area, high-sensitivity design. This low-pass filter is applied directly to signals generated by the counter (neutron pulses and gamma pileup). It reduces the peak amplitudes of both neutron and gamma pulses by equivalent amounts because of their similar shapes. In addition, both types of pulses are similarly stretched. The increased width is of no consequence for individual neutron pulses at the input of an amplitude-sensitive discriminator, but the longer pulse widths enhance the gamma pileup. Therefore, the net effect of this filter is to reduce the neutron-to-gamma pileup signal ratio. Since the electronic noise is generated at the preamplifier input, it is not affected by this filter, although the counter end of the input cable presents a mistermination that causes a resonant structure in the preamplifier noise spectrum. It has been our experience that this resonant structure can be neglected.

Figure 10 shows the influence of cable impedance for two values of C_c (270 and 1100 pF) to simulate two different electrode areas. The filter time constant was 27 ns. Only the case for the 4-mm spacing at an E/P value of 1.38 was studied. The low-capacitance data show that the

25-Ω cable provided ∿15% more neutron sensitivity than the 16.7-Ω cable and nearly 10% more sensitivity than the widely used value of 50 Ω.

The trend of the higher capacitance data is qualitatively similar to that of the low-capacitance case. Here, the 16.7- and 25-Ω cables gave equivalent performance, with nearly 15% more sensitivity than the 50-Ω case.

With only three data points, it is difficult to predict precisely the cable impedance corresponding to the maximum figure of merit. Noting that the maxima tend to be broad, we observe that the data indicate a maximum above 25 Ω in the low-capacitance case and below 25 Ω in the high-capacitance case. We expect this result because the higher capacitance allows the cable impedance to be reduced to lower values before gains in the ratio of the neutron pulse amplitude to the gamma pileup are offset by increasing electronic noise, as previously mentioned in connection with the discussion of PD product.

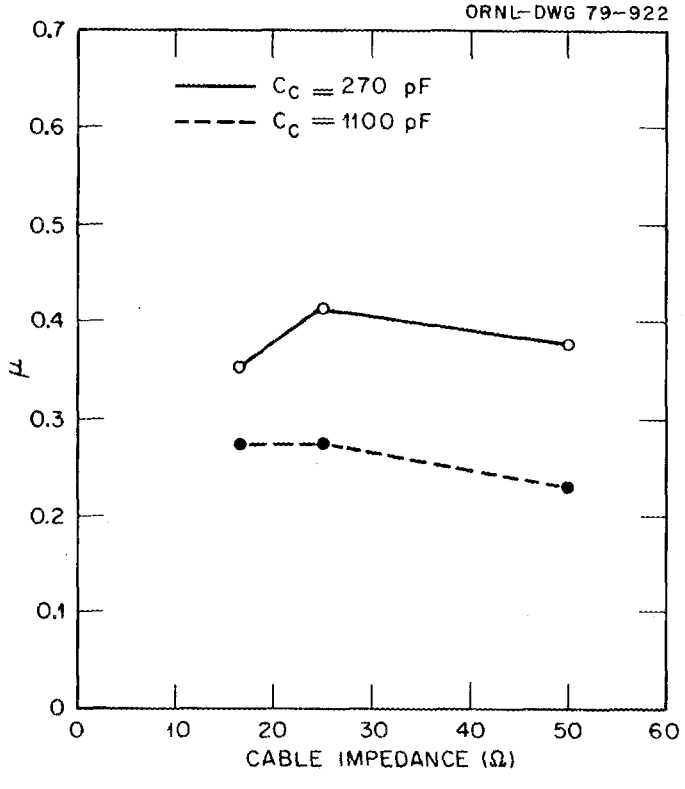

Fig. 10. Experimental figure of merit versus cable impedance for two values of interelectrode capacitance (Ar - 5% CO_2, at 724 torr, 1.6×10^6 R/h, E/P = 1.38 V $torr^{-1}$ cm^{-1}, τ_f = 27 ns, D = 4 mm).

9.5 Filter Time Constant and Gamma Dose Rate

Figure 11 shows the figure of merit at three different gamma dose rates and two RC-CR time constants of 13 and 50 ns. The fill gas was Ar - 10% CO_2 at 724 torr; the other variables were constant at Z_0 = 50 Ω, E/P = 2.0 V $torr^{-1}$ cm^{-1}, and D = 4 mm. The interesting point is that, whereas the larger filter time constant gave the better performance at zero gamma dose rate where electronic noise is the dominant noise source, the shorter time constant was superior for operation in the high gamma fields. These data show that a counter which is optimized for operation at a particular gamma dose rate does not necessarily represent an optimum design at a different dose rate. In fact, the analysis can be used to demonstrate that a given design can represent an optimum only at a unique value of gamma dose rate.

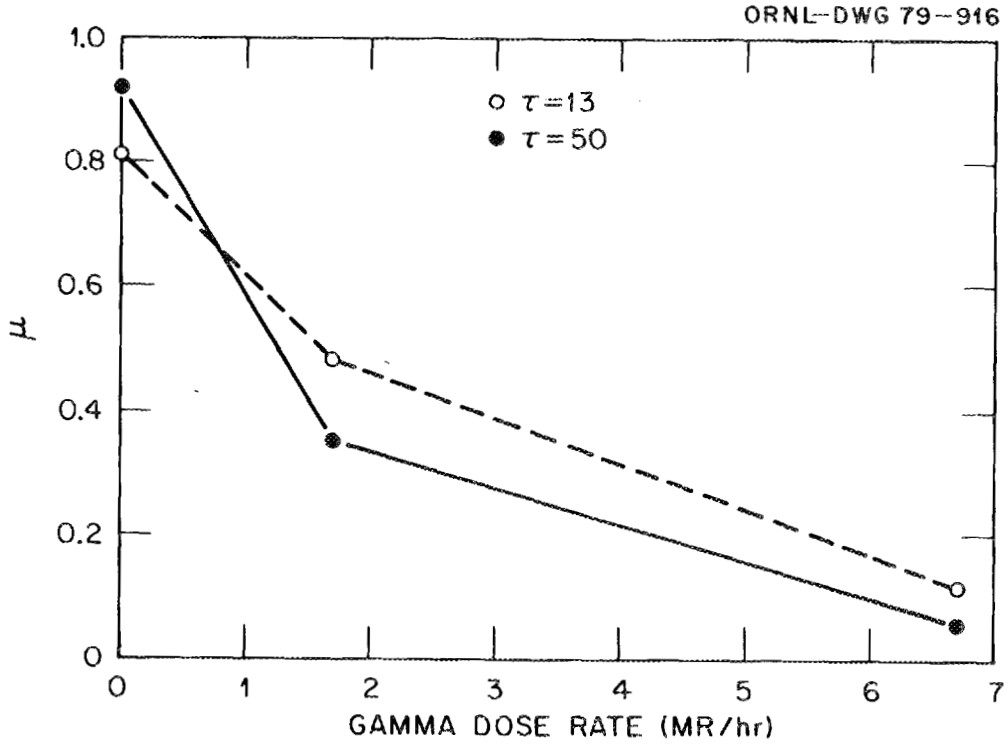

Fig. 11. Experimental figure of merit versus gamma dose rate for two values of filter time constant (Ar - 10% CO_2, at 724 torr, Z_o = 50 Ω, E/P = 2.0 V $torr^{-1}$ cm^{-1}, D = 4 mm).

By noting that the left-hand factor in the right-hand side of Eq. (15) is totally independent of D and τ_f, we see that values of D and τ_f that maximize or optimize the right-hand factor also optimize μ'. These values, which satisfy

$$\frac{\partial \mu'}{\partial \alpha} = \frac{\partial \mu'}{\partial \beta} = 0 \ , \tag{18}$$

are plotted in Fig. 12 as a function of σ_{p0}/σ_{e0}. The optimized quantity, $\left(k\sigma_{e0}\tau_0^{1/2}/q_n\right) \times \mu'$ is plotted in Fig. 13.

Several important qualitative trends are indicated in Figs. 12 and 13. It is evident from Fig. 12 that as the design gamma dose rate increases (i.e., as σ_{p0}/σ_{e0} increases) the best performance will be obtained from smaller electrode spacings (implying faster collection times) and higher filter breakfrequencies. Figure 13 shows that the performance decreases monotonically with increasing gamma dose rate. All three of these trends are in accord with a relatively vast body of design experience, and thus they provide some credibility to the analysis.

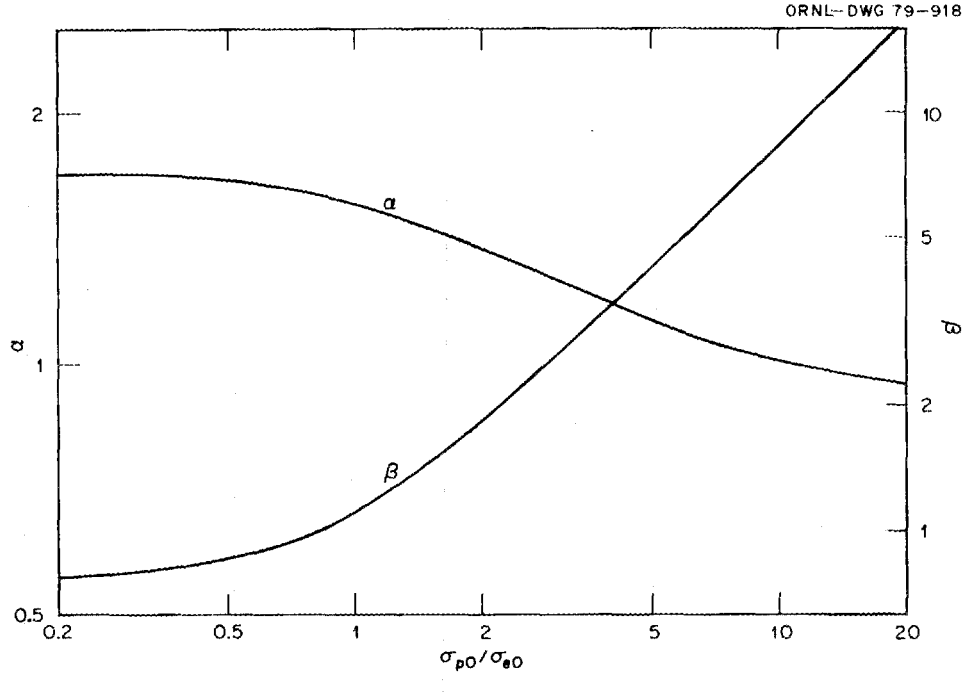

Fig. 12. Computed optimum values of dimensionless electrode spacing (α) and dimensionless filter time constant (β) versus the ratio of gamma pileup to electronic noise.

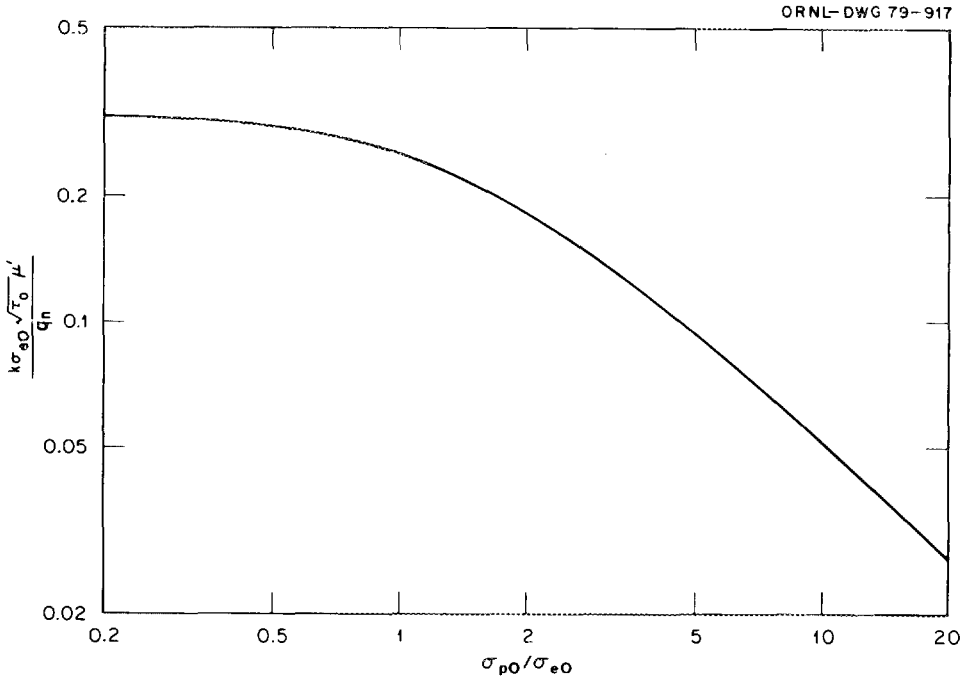

Fig. 13. Computed dependence of the figure of merit on the ratio of gamma pileup to electronic noise.

9.6 E/P Ratio

The effect of the E/P ratio is shown in Fig. 14 for three different fill gases -- Ar - 10% CO_2, Ar - 5% CO_2, and Ar - 10% N_2. For each fill gas, the only variable was E/P. Since the counter was well saturated during measurements, the variations in the figure of merit can be attributed directly to variations in the electron drift velocity. In fact, a comparison of these curves to those of Fig. 15, in which the electron drift velocity is plotted as a function of E/P for these gas mixtures, shows striking similarities.

The most obvious result of the comparison is that the figure of merit appears to be directly related to the drift velocity. In this case, both the figure of merit data and the drift velocity curves indicate that the electron drift velocity in an Ar - 5% CO_2 mixture saturates at a lower E/P ratio value than in a 10% CO_2 mixture. In addition, both indicate that an Ar - 10% N_2 mixture has the slowest drift velocity in the E/P range considered. The drift velocity curves of Fig. 15 are somewhat

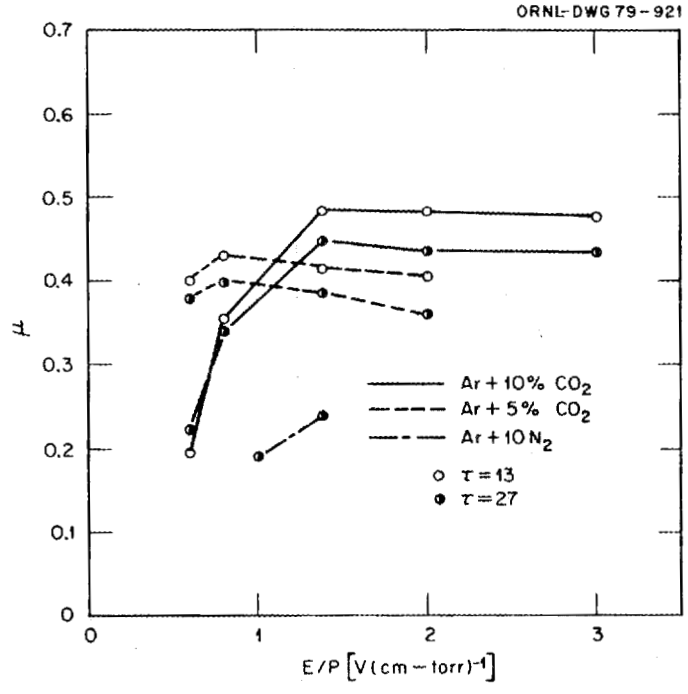

Fig. 14. Experimental figure of merit versus E/P for 4-mm electrode spacing and 1.6×10^6 R/h gamma dose rate.

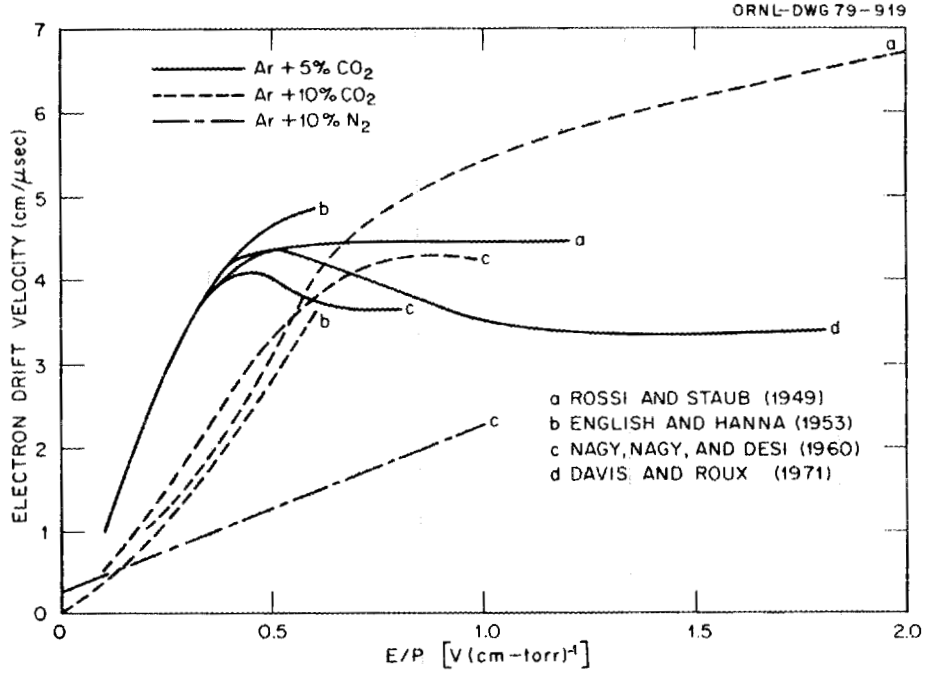

Fig. 15. Measured electron drift velocity curves for three counting gas mixtures.

ambiguous concerning which CO_2 mixture has the fastest saturated drift velocity. However, the data of Fig. 14 remove the ambiguity, clearly showing that the drift velocity in the 10% mixture is the faster.

Referring to Fig. 13, an interesting result can be obtained by noting that once σ_{p0} is set, the optimized value of μ' is proportional to $q_n/k\sigma_{e0}\tau_0^{1/2}$. The only dependence on drift velocity in this multiplier is contained in $\tau_0 = \left(\varepsilon_o AZ_0/v_d\right)^{1/2}$. Thus, since for optimized designs μ' is proportional to $\left(v_d/\varepsilon_o AZ_0\right)^{1/4}$, the performance should increase directly as the one-fourth power of the drift velocity and inversely as the one-fourth power of the electrode area (i.e., good performance becomes increasingly difficult to achieve as the electrode area is increased).

10. CONCLUSIONS

Several trends can be inferred from this study, some of which confirm previously known relationships between design variables and counter performance. Most important is the proved existence of an optimum electrode spacing for a specific design that increases with electrode area and decreases with gamma dose rate. The PD product also has an optimum value, with low values being limited by the presence of electronic noise and high values by enhanced gamma pileup. Conventional 50-Ω signal cables do not always provide the best performance, particularly for large-area counters that have high interelectrode capacitances and operate in high gamma background. Values as low as 16.7 Ω yield an improvement of as much as 20%. The performance of a counter closely follows the E/P versus drift velocity characteristic of its gas mixture, and is superior for fill gases having higher electron drift velocities. The optimum filter time constant of the counting channel depends on the gamma background dose rate. At low gamma levels, when electronic noise dominates, longer filter time constants give better signal-to-noise ratios. Counters with shorter collection times more effectively suppress the gamma pileup at high dose rates, and filters with higher break-frequencies process the faster pulses more effectively.

Another conclusion from this study is that the usable neutron sensitivity per gram of neutron-sensitive material is a monotonically decreasing function of electrode area. These sensitivity losses can be minimized for high-sensitivity fission counters by use of neutron-sensitive material with low intrinsic alpha activity (such as electromagnetically enriched uranium), as well as by careful specification of the major design variables.

REFERENCES

1. V. K. Paré, *Model of a Fission Counter System for Optimizing Performance at High Gamma Dose Rates*, ORNL/TM-6408 (November 1978).
2. W. Abson et al., "The Design, Performance and Use of Fission Counters," *Proc. Inst. Elec. Engrs., (London)* 105B, 349 (1958).
3. J. T. De Lorenzo, W. T. Clay, and G. C. Guerrant, "Differential Current Pulse Preamplifier for Fission Counters," *IEEE Trans. Nucl. Sci.* NS-21, 757-762 (1974).
4. J. T. De Lorenzo, "Fast Differential Discriminator," p. 14 in *Instrumentation and Controls Div. Bienn. Prog. Rep. Sept. 1, 1976, to Sept. 1, 1978*, ORNL-5483 (November 1978).
5. N. C. Hoitink and L. D. Philipp, *Effects of Gas Mixture, Electrode Spacing, Gas Pressure and Applied Voltage on the Gamma Performance of Fission Counters*, HEDL-SA-442 (October 1972).
6. J. T. De Lorenzo, "Low-Noise, Wide-Band, Current-Pulse Preamplifier for Neutron Counters," *IEEE Trans. Nucl. Sci.* NS-19 (2), 114-116 (April 1971).

ORNL/TM-6926
Dist. Category
Uc-79 and -79m

INTERNAL DISTRIBUTION

1. R. S. Booth
2. M. M. Chiles
3-7. W. T. Clay
8-12. J. T. De Lorenzo
13-17. G. C. Guerrant
18. R. C. Kryter
19. C. D. Martin
20. J. T. Mihalczo
21. L. C. Oakes
22-26. V. K. Paré
27. G. L. Ragan
28. C. W. Ricker
29. G. S. Sadowski
30. C. M. Smith
31-35. K. H. Valentine
36-37. Central Research Library
38. Document Reference Section
39-41. Laboratory Records
42. Laboratory Records ORNL RC
43. ORNL Patent Office

EXTERNAL DISTRIBUTION

44-45. Director, Division of Reactor Development and Demonstration, Department of Energy, Washington, D.C. 20545

46. Director, Reactor Division, Oak Ridge Operations Office, P. O. Box E, Oak Ridge, Tennessee 37830

47. Asst. Manager, Energy Research & Development, DOE-ORO

48-235. Given distribution as shown in TID-4500 for categories UC-79 and -79m (25 copies - NTIS)